Journal of Photochemistry and Photobiology A: Chemistry 216 (2010) 183–193

Contents lists available at ScienceDirect

Journal of Photochemistry and Photobiology A: Chemistry

journal homepage: www.elsevier.com/locate/jphotochem

Novel (and better?) titania-based photocatalysts: Brookite nanorods and mesoporous structures

Adel A. Ismail[a,b], Tarek A. Kandiel[b], Detlef W. Bahnemann[b,*]

[a] Advanced Materials Department, Central Metallurgical Research and Development Institute, CMRDI, Helwan, Egypt
[b] Photocatalysis and Nanotechnology, Institut für Technische Chemie, Leibniz Universität Hannover, Callinstrasse 3, D-30167 Hannover, Germany

ARTICLE INFO

Article history:
Available online 31 May 2010

Keywords:
Titanium Dioxide
Photocatalysis
Brookite nanorods
Anatase nanoparticles
Mesoporous structure
DCA degradation
Hydrogen production
Methanol photooxidation

ABSTRACT

Herein, recent results concerning the synthesis of tailored anatase/brookite mixtures and of pure brookite TiO_2 nanorods will be reported employing a simple hydrothermal method, i.e., the reaction of aqueous solutions of the titanium(IV) bis(ammoniumlactate) dihydroxide complex with urea. Highly ordered hexagonal *P6m* mesoporous Pd or Au doped TiO_2 nanocomposites have also been synthesized using the F127 triblock copolymer as a template. Utilizing these nanomaterials, the effect of the phase composition, the role of the surface area, and of the ordered mesoporous structure on the photocatalytic activity of titania-based photocatalysts have been investigated. The results revealed that anatase/brookite mixtures and brookite nanorods exhibit higher photocatalytic activity than anatase nanoparticles and even higher than Aeroxide (Evonik) TiO_2 P25 for the photocatalytic H_2 evolution from aqueous methanol solution, despite the fact that the former have lower surface areas. This behavior is explained by the fact that the flatband potential of brookite nanorods is shifted by 140 mV more cathodically than the flatband potential of anatase nanoparticles and/or by the better charge carrier separation in the case of anatase/brookite mixtures. Hexagonal *P6m* mesoporous Au and Pd/TiO_2 nanoarchitectures showed ~3–4 times higher activity for the photooxidation of CH_3OH than Pd photodeposited on commercial Sachtleben Hombikat UV-100. The increased HCHO formation rate revealed that the photocatalytic oxidation efficiencies within the mesoporous Pd/TiO_2 system are (in spite of its lower surface area) superior to that of Pd/UV-100. The key to this success is the preparation of Pd/TiO_2 networks with an ordered mesoporous structure which at the same time render the methanol diffusion into the bulk of the photocatalysts facile and hence provide fast transport channels for the methanol molecules.

1. Introduction

TiO_2 nanomaterials exhibiting different morphologies and polymorphs have recently attracted great interest, as their optical and electrical properties strongly depend on shape, size, phase composition, and the design of the nanostructures [1–3]. It is well known that crystalline TiO_2 exists in three polymorphs: anatase (A), rutile (R), and brookite (B). Each phase displays different physical and chemical properties exhibiting different functionalities. As a bulk material, rutile is the thermodynamically stable phase; however, solution-phase preparation methods for TiO_2 generally favor the anatase structure. Since most of the synthetic processes produce anatase, rutile or a mixture of them, both phases are readily employed for practical applications and have been extensively studied as photocatalysts. On the other hand, the brookite phase is rarely being studied [4–8] mainly due to the difficulties encountered in obtaining its pure form, however, it was reported that brookite nanocrystals have markedly higher photocatalytic activities as compared to those of rutile and anatase [9].

Besides the effect of TiO_2 phase compositions on the photocatalytic activity, mesoporous TiO_2 nanomaterial has also proven to be a good candidate as a photocatalyst. However, in most cases, the mesoporosity is a result of the agglomeration of TiO_2 nanoparticles. The preparation of highly ordered mesoporous TiO_2 can therefore still be regarded as a challenge. Mesoporous TiO_2 is an interesting material for photocatalytic applications due to its continuous network of particles, which may be beneficial compared to separated individual nanoparticles, in particular for catalyst recovery. Usually, mesoporous TiO_2 is prepared by template-based methods using soft templates (surfactant and block polymers) and hard templates (porous silica, polystyrene spheres, porous carbon) [10–13]. However, the wall of these materials is normally amorphous, and upon heat treatment, crystallization results in the collapse of the uniform mesoporous structure. TiO_2 has been widely used as a photocatalyst for the removal of hazardous organic substances and as an electrode material for dye-sensitized solar cells [14,15] due to

* Corresponding author. Tel.: +49 511 762 5560; fax: +49 511 762 2774.
E-mail address: bahnemann@iftc.uni-hannover.de (D.W. Bahnemann).

1010-6030/$ – see front matter © 2010 Elsevier B.V. All rights reserved.
doi:10.1016/j.jphotochem.2010.05.016

its strong oxidizing and reducing ability under UV light irradiation. Two of the most important factors affecting the photocatalytic activity of TiO_2 are its specific surface area in a continuous structure rather than in discrete particles and its crystallinity. The structure continuity can be expected to facilitate the electron transfer within the material, resulting in higher activity. If mesoporous TiO_2 could be prepared consisting of anatase crystallites, it can be expected to be a useful material exhibiting a high performance as a photocatalyst. Also, it has been demonstrated that the addition of a low percentage of precious metals, such as Pt, Ag, Pd, and Au [16–20] to TiO_2 improves its photocatalytic activity.

Herein, we report facile synthesis methods for the preparation of anatase nanoparticles, tailored anatase/brookite mixtures, brookite TiO_2 nanorods, and of highly ordered hexagonal *P6m* mesoporous Au or Pd/TiO_2 nanocomposites. Utilizing these nanomaterials, the effect of the phase composition, the role of the surface area, and of the ordered mesoporous structure on the photocatalytic activity of titania-based photocatalysts has been investigated. The photocatalytic activities of these newly prepared photocatalysts have also been compared with those of the commercial photocatalysts, i.e., Sachtleben Hombikat UV-100 and Evonik Aeroxide TiO_2 P25.

2. Experimental

2.1. Materials

Titanium(IV) bis(ammoniumlactate) dihydroxide (TALH, 50% aqueous solution), $H_2PtCl_6{\cdot}6H_2O$ (Alfa Aesar) and $(NH_2)_2CO$ (Aldrich) were used as received. The block copolymer surfactant EO_{106}-$PO_{70}EO_{106}$(F-127, EO = $-CH_2CH_2O-$, PO = $-CH_2(CH_3)CHO-$), MW 12,600 g mol^{-1}), $Ti(OC(CH_3)_3)_4$ (TBOT), HCl, CH_3OH, C_2H_5OH, CH_3COOH, $HAuCl_4{\cdot}4H_2O$ and K_2PdCl_4 were purchased from Sigma–Aldrich and used as received. Commercial TiO_2 (Hombikat UV-100, 100% anatase) was kindly provided by Sachtleben Chemie GmbH. Aeroxide TiO_2 P25 (82% anatase and 18% rutile) was a gift from Evonik, Germany.

2.2. Preparation of TiO_2 photocatalysts

2.2.1. Hydrothermal preparation of anatase nanoparticles, anatase/brookite mixtures, and brookite nanorods

Anatase nanoparticles, anatase/brookite mixtures and brookite nanorods have been prepared as previously described [21]. Briefly, 10 ml of the aqueous TALH precursor and an aqueous solution containing the desired amount of urea were mixed followed by the addition of deionized water to reach a final volume of 100 ml. The resulting solution was transferred into a Teflon cup (250 ml). Afterwards, the Teflon cup was sealed in a stainless steel autoclave (Berghof, DAB-3) and placed into an electric furnace held at 160 °C for a required time. Then, the autoclave was cooled in air. The resulting powders were separated by centrifugation, washed three times with water, and dried overnight at 60 °C in an oven. The yield is found to be not <97% of the expected yield calculated from the complete thermal hydrolysis of the available TALH complex.

2.2.2. Preparation of Au/TiO_2 and Pd/TiO_2 nanocomposites

To minimize possible variables, the molar ratio of each reagent in the starting solution was fixed at TiO_2/F127/C_2H_5OH/HCl/CH_3COOH = 1:0.02:50:2.25:3.75 mol l^{-1} ratios. In particular, 1.6 g of F127, 2.3 ml of CH_3COOH and 0.74 ml of HCl were dissolved in 30 ml of ethanol and then added to 3.5 ml of TBOT. The calculated amount of either $HAuCl_4{\cdot}4H_2O$ or K_2PdCl_4 was added to the F127-TBOT-CH_3COOH mesophase to obtain 0.5 wt.% noble metals/TiO_2 and the mixture was stirred vigorously for 60 min and transferred into a Petri dish. The height of the sol in the Petri dish (diameter 20 cm) was 5 mm. Ethanol was subsequently evaporated at 40 °C and a relative humidity of 40% for 12 h followed by the transfer of the sample into a 65 °C oven and ageing for an additional 24 h. The as-made mesostructured hybrids were calcined at 300–550 °C in air for 4 h at a heating rate of 1 °C min^{-1} and a cooling rate of 2 °C min^{-1} to remove the surfactant and to obtain highly ordered mesostructured Au/TiO_2 or PdO/TiO_2, respectively. Subsequently, the PdO/TiO_2 materials were subjected to H_2 gas for 2 h at 300 °C to obtain ordered hexagonal *P6m* mesoporous Pd/TiO_2.

2.3. Characterization

XRD data for the Rietveld phase analysis of TiO_2 have been recorded on a Phillips PW1800 diffractometer using a reflection geometry with variable divergence slits, Cu $K\alpha_{1,2}$ radiation and a secondary monochromator. Three thousand data points were collected with a step width of 0.02° and 2 s measurement time per step in the 2θ range from 20° to 80°. The phase analysis by the Rietveld method was carried out using the TOPAS 2.0 (Bruker AXS) software. During the refinements general parameters, such as scale factors, one background parameter and the zero point error were optimized. Profile shape calculations were carried out on the basis of standard instrumental parameters using the fundamental parameter approach implemented in the program, also varying the average crystal size (integral breadth) of the reflections. Lattice parameters and crystallite size of all phases were refined. Structural data for the known phases were taken from the PDF-2 database with PDF numbers: anatase [21-1272], rutile [21-1276], and brookite [29-1360]. Small angle X-ray diffraction (SAXRD) patterns were recorded on a Bruker D8 advance instrument.

Field-emission-scanning electron microscopy (FE-SEM) measurements were carried out on a JEOL JSM-6700F field-emission instrument using a secondary electron detector (SE) at an accelerating voltage of 2 kV. Transmission electron microscopy (TEM) was conducted at 200 kV with a JEOL JEM-2100F-UHR field-emission instrument equipped with a Gatan GIF 2001 energy filter and a 1k-CCD camera in order to obtain EEL spectra.

Single-point standard BET surface area measurements were carried out employing a Micromeritics AutoMate 23 instrument. The gas mixture used for the adsorption determinations was 30% nitrogen and 70% helium. The TiO_2 samples were previously heated to 150 °C for approximately 60 min in order to clean the surface of adsorbed organic compounds and humidity. The nitrogen adsorption and desorption isotherms at 77 K were measured using a Quantachrome Autosorb 3B after the samples were vacuum-dried at 200 °C overnight. The sorption data were analyzed using the Barrett–Joyner–Halenda (BJH) model with the Halsey equation [22].

2.4. Assessment of the photocatalytic activities

Photocatalytic molecular hydrogen production: the photocatalytic molecular hydrogen production tests have been performed in a double jacket Duran glass reactor (110 cm^3) with three outlets as described elsewhere [23]. The inner part of the reactor is a cylindrical tube with a diameter of 4 cm and a height of 6.0 cm. In a typical run, 0.0375 g of the photocatalyst powder have been suspended in 75 ml of an aqueous methanol solution (4.92 mol l^{-1}) by sonication. The suspension was transferred to the photoreactor and bubbled with Ar for 30 min to remove any dissolved O_2. The reactor was sealed with a silicone rubber septum and repeatedly flushed with Ar for another 30 min until no O_2 and N_2 were detected by gas chromatography in the headspace above the solution. Subsequently, the stopcocks were closed and the photoreactor was connected to the cooling system. The photoreactor was irradiated from the outside using an Osram XBO 1000 W Xenon lamp in a Müller LAX 1000 lamp

housing. The evolved gas was sampled at a constant rate through the silicone rubber septum using a locking-type syringe. The sampled gas was quantitatively analyzed using a gas chromatograph (Shimadzu 8A, TCD detector). The GC was equipped with a molecular sieve 5 Å packed column for hydrogen analysis. Ar was used as the carrier gas.

The incident photon flux in the wavelength range $300\,nm \leq \lambda \leq 400\,nm$ was determined by ferrioxalate actinometry to be 3.62×10^{-7} einstein s^{-1} [24,25]. The lamp was switched on 30 min before the beginning of the reaction to stabilize the power of its emission spectrum. The actinometry was performed in the same photochemical reactor with the same volume of actinometric solution as the photocatalytic test, eliminating possible errors associated with the influence of light reflections and reactor geometry. A water bath and a black bandpass filter (3 mm, UG1 SCHOTT glass) were used during photon flux and photonic efficiency measurements.

Photocatalytic dichloroacetic acid (DCA) degradation: the photocatalytic DCA degradation has been measured in a 60 ml double jacket quartz glass reactor. In typical run, 0.03 g of the photocatalyst were suspended in 60 ml of aqueous 10 mmol l^{-1} KNO_3 by sonication before the addition of DCA into the slurry (initial DCA concentration 1.0 mmol l^{-1}). The pH was then adjusted to pH 3 by addition of 0.1 mol l^{-1} HNO_3 or NaOH as needed. The temperature of the suspension was maintained at 25 °C. The suspension was vigorously stirred without illumination for 30 min to attain the adsorption equilibrium of the DCA molecules on the photocatalyst surface and continuously purged with air to ensure a constant O_2 concentration throughout the experiment. After this adsorption period, UV illumination was provided by a high-pressure Xe-lamp (OSRAM HBO 450 W). A UV(A)–vis illumination was achieved employing a cut-off filter (WG 320) which eliminates UV-radiation below $\lambda = 320$ nm. The intensity of UV(A) illumination was 60 mW cm^{-2} at the entrance window of the photoreactor as measured by a UV light meter (ultraviolet radiometer LTLutron UVA-365).

The photocatalytic degradation of dichloroacetic acid was measured at pH 3. The pK_a of DCA is 1.29, and it thus exists in its anionic form in aqueous solutions at pH > 2. The photocatalytic oxidation of one DCA anion results in the formation of one proton, two CO_2 molecules, and two Cl^- ions according to Equation (1). The pH of the suspension was maintained constant during the photocatalytic experiments using a pH-stat technique as described by Bahnemann et al. [26].

$$CHCl_2COO^- + O_2 \xrightarrow{h\nu,\ TiO_2} 2CO_2 + H^+ + 2Cl^- \quad (1)$$

The rate of the photodegradation of DCA was followed by measuring the amount of OH^- added to keep the pH constant thus measuring the amount of H^+ formed which is equivalent to the amount of DCA degraded. The mineralization of DCA was confirmed by TOC measurements at the end of the experimental runs. In all runs, more than 90% DCA removal was observed. The photonic efficiencies (ζ) of the photocatalytic degradation of DCA were calculated as the ratio of the initial degradation rate of DCA and the incident photon flux according to Equations (2) and (3), where the initial degradation rate is calculated from the slope of the individual concentration vs. time profiles. The incident photon flux per volumetric unit has been calculated to be 3.31×10^{-2} einstein l^{-1} h^{-1} based upon the UV-A light meter measurements and assuming an average illumination wavelength $\lambda = 350$ nm; the irradiated surface area was 3.14 cm^2, and the volume of the suspension was 0.06 l.

$$I_0 = \frac{I \cdot \lambda}{N_A \cdot h \cdot c} \quad (2)$$

$$\zeta(\%) = \frac{k \cdot c_0 \cdot V}{I_0 \cdot A} \cdot 100 \quad (3)$$

(with I_0, being the photon flux; I, the light intensity; N_A, Avogadro's number; h, the Planck constant; c, the light velocity; k, the initial rate constant; A, the illuminated area; c_0, the initial DCA concentration; λ, the illumination wavelength; and V, the reactor volume).

Photocatalytic oxidation of methanol: a quartz photoreactor was filled with 75 ml aqueous solution of methanol at a concentration 30 mmol l^{-1}. UV irradiation was performed by a 450 W medium pressure xenon lamp (Osram) placed inside a quartz jacket and equipped with a cooling tube. The lamp was switched on 30 min prior to the start of the reaction to stabilize the power of its emission at $\lambda > 320$ nm (a cut-off filter was used to remove light with wavelengths below 320 nm) and the reactor was cooled by circulation of water. The temperature of the cooling water was stabilized to perform the reactions at 25 °C. Photooxidation reactions were carried out suspending 1 g l^{-1} of the prepared photocatalysts with oxygen being purged through the reaction vessel continuously. The aqueous suspensions were sonicated in the presence of the desired amount of methanol [30 mmol l^{-1}] before the experiment was started and were subsequently stirred in the dark for 30 min to reach the adsorption equilibrium. Aliquots were withdrawn at regular intervals from the upper part of the reactor for HCHO analysis with the catalyst being removed from the liquid phase by filtration through nylon syringe filters (pore size: 0.45 μm). The photooxidation rate was determined by measuring the amount of HCHO generated as a result of the methanol oxidation during the first 60 min of illumination employing the Nash method [27]. The detection limit for HCHO determined by the Nash method is 1.66 μmol l^{-1}. The relative error of the measured HCHO concentration was ±5% as judged from repeated runs under identical conditions. This method is based on the reaction of formaldehyde with acetylacetone and ammonium acetate to form a yellow coloured product with a maximum of absorbance at 412 nm. Measurements were carried out using a Varian Cary 100 Scan UV-vis spectrophotometer, following an incubation time of 15 min at 60 °C. The photonic efficiency was calculated for each experiment as the ratio of the HCHO formation rate and the incident light intensity as given in the following equation: $\zeta = (r \times 100/I_0)$ [28], where ζ is the photonic efficiency (%), r is the photooxidation rate of methanol (mol l^{-1} s^{-1}), and I_0 is the incident photon flux (4.94×10^{-6} einstein l^{-1} s^{-1}). The UV-A incident photon flow was determined by ferrioxalate actinometry [24,25].

3. Results and discussion

3.1. Characterization of TiO_2 photocatalysts

Anatase nanoparticles, anatase/brookite mixtures and brookite nanorods: the thermal hydrolysis of the TALH precursor at 160 °C for 24 h in the presence of 0.1 mol l^{-1} urea yields pure anatase nanoparticles; whereas with increasing concentration of urea up to 2.0 mol l^{-1}, biphasial anatase/brookite mixtures are formed. At higher urea concentration (6.0 mol l^{-1}), high quality brookite is obtained as proven by XRD measurements (see Fig. 1). The existence of brookite in the resultant powders is readily discernible from its (1 2 1) diffraction located at 30.81° (2θ) in the XRD pattern, where no overlapping of this peak with any peak from anatase or rutile occurs. To claim phase pure brookite, however, attention should be paid to the reflections in which overlapping with anatase reflections can occur. This is especially important for the (1 0 1) reflection of anatase and the (1 2 0) reflection of brookite. The diffraction data were analyzed by the Rietveld method considering the whole pattern and not only single peaks. Thus, a higher sensitivity for low phase contents is possible even when peak broadening due to small crystallite sizes occurs. The Rietveld analysis proofs that no anatase is present in the powders synthesized via this new

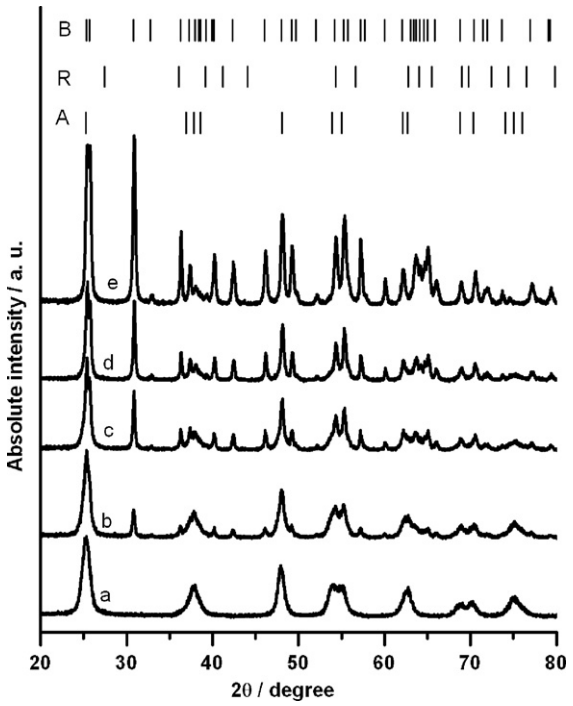

Fig. 1. XRD patterns of as-synthesized nanocrystalline TiO_2 powders obtained by thermal hydrolysis of aqueous solutions of the TALH precursor at 160 °C for 24 h in the presence of different concentrations of urea, (a) 0.1 mol l^{-1}, (b) 1.0 mol l^{-1}, (c) 1.5 mol l^{-1}, (d) 2.0 mol l^{-1}, and (e) 6.0 mol l^{-1}; labels B, R and A indicate Bragg positions for brookite, rutile, and anatase, respectively. (Adapted with permission from ref. [21]. Copyright 2010 American Chemical Society).

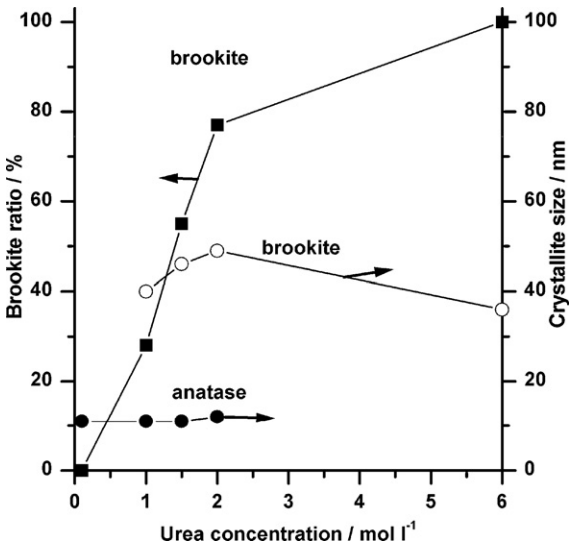

Fig. 2. Plotting of brookite ratios and crystallite sizes as evident from the Rietveld analysis of the XRD data vs. concentration of urea.

procedure employing 6.0 mol l^{-1} urea in the synthesis step. The small diffraction peak observed at 74.5° (2θ) (cf. Fig. 1e) can readily be explained by the (1 0 4) diffraction of brookite. The quantitative phase composition and crystallite diameters of the nanocrystalline TiO_2 powders as evident from the Rietveld analysis of the XRD data are illustrated in Fig. 2.

To obtain information about the particles morphology, some selected powders were investigated by field-emission-scanning

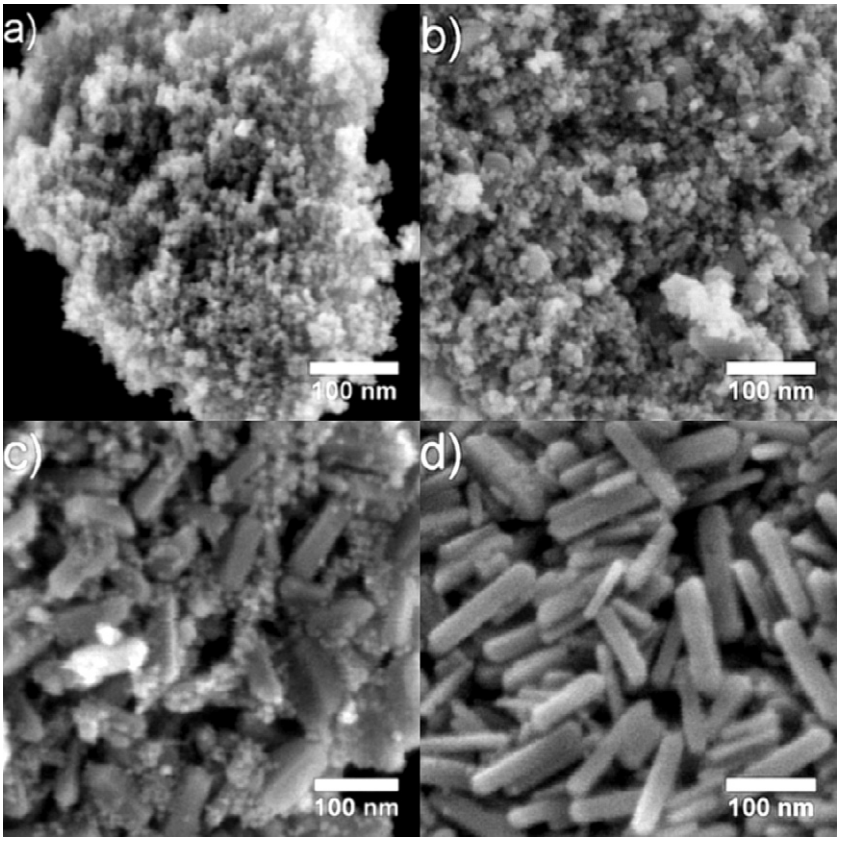

Fig. 3. FE-SEM micrographs of as-synthesized nanocrystalline TiO_2 powders obtained by thermal hydrolysis of aqueous solutions of the TALH precursor at 160 °C for 24 h in the presence of different concentrations of urea, (a) 0.1 mol l^{-1}, (b) 1.0 mol l^{-1}, (c) 2.0 mol l^{-1}, and (d) 6.0 mol l^{-1}. (Reprinted with permission from ref. [21]. Copyright 2010 American Chemical Society).

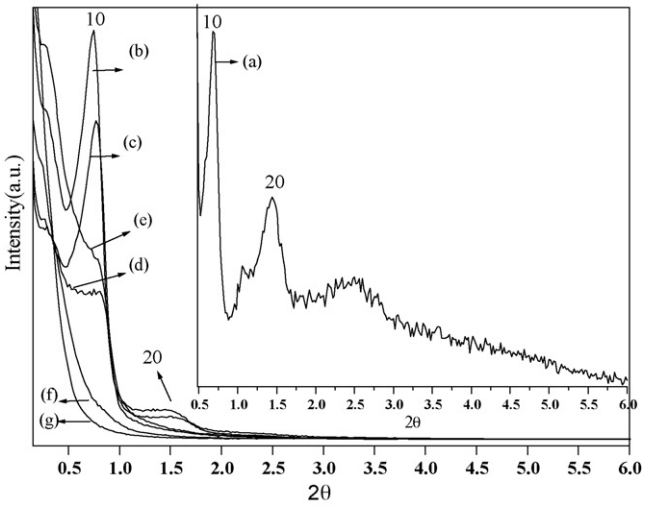

Fig. 4. SAXRD patterns of as made Pd/TiO_2 (a) (inset) and calcined at 300 °C (b), 350 °C (c), 400 °C (d), 450 °C (e), 500 °C (f) and 550 °C (g). (Adapted with permission from ref. [20]. Copyright 2010 American Chemical Society)

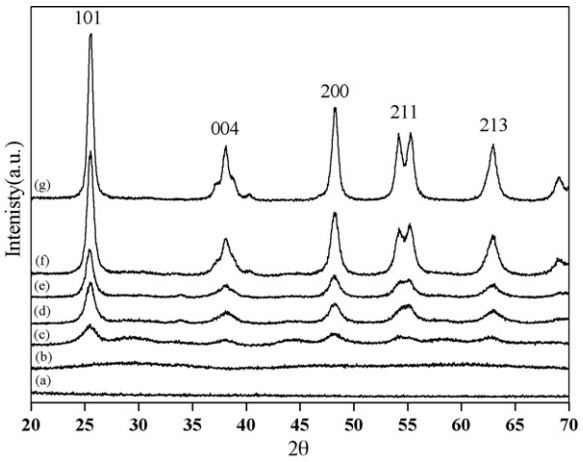

Fig. 5. WXRD of as made Pd/TiO_2 (a) and calcined at 300 °C (b), 350 °C (c), 400 °C (d), 450 °C (e), 500 °C (f) and 550 °C (g). (Adapted with permission from ref. [20]. Copyright 2010 American Chemical Society).

electron microscopy (FE-SEM). The micrographs of the anatase TiO_2 powder obtained by thermal hydrolysis of the TALH precursor at 160 °C for 24 h in presence of 0.1 mol l^{-1} of urea indicate that the pure anatase powder aggregates from fine TiO_2 nanoparticles in the size range of 10 nm (as shown in Fig. 3a) in good agreement with the particle size predicted from the XRD analysis. Fig. 3b and c shows the micrographs of two different biphasial anatase/brookite mixtures, (72% anatase and 28% brookite) and (23% anatase and 77% brookite), respectively. Both micrographs indicate the formation of small nanoparticles in the size range of 10 nm and rod-like nanoparticles with diameters in the range of 25 nm. Fig. 3d shows the micrograph of pure brookite obtained by the thermal hydrolysis of the TALH precursor at 160 °C for 24 h in the presence of 6.0 mol l^{-1} of urea, evincing that TiO_2 nanorods with diameters up to 25 nm and lengths up to 150 nm are formed. From XRD crystallite size data and SEM micrographs it could be concluded that the small nanoparticles crystallize in the anatase phase while the nanorods consist of brookite, however, by definition, the crystallite size derived from the XRD analysis does not necessarily match the particle size observed by SEM.

Mesoporous TiO_2 photocatalysts: highly ordered Au/TiO_2 or Pd/TiO_2 nanocrystals, respectively, were synthesized through a simple one-step sol–gel process in the presence of the F127 triblock copolymer as structure directing agent. To homogenously distribute Au and Pd nanoparticles into the TiO_2 framework, a multicomponent assembly approach was utilized, where surfactant, TiO_2, and Pd or Au were assembled in a one-step process. Fig. 4 displays the small angle X-ray diffraction (SAXRD) patterns of highly ordered mesoporous Pd/TiO_2 as-made and of calcined samples. The as-made sample shows two well-resolved peaks, which can be indexed to the (1 0) and (2 0) Bragg reflections confirming an ordered 2D-hexagonal mesostructure of the *P6m* space group [29]. The observed high intensities and the sharpness of the peaks prove that a long-range order exists in the Pd/TiO_2 nanoarchitectures. With increasing calcination temperature the diffraction peaks are becoming weaker with the (1 0) and (2 0) reflections indicating that the long-range ordering of the mesopores is already disappearing for the samples calcined at 450 °C. Fig. 5 shows the wide-angle XRD patterns of the as-made and calcined samples. The as-made sample is amorphous since no distinct reflections can be observed. The calcined samples exhibit five distinct peaks characteristic for the (1 0 1), (0 0 4), (2 0 0), (2 1 1) and (2 1 3) phases contributed by anatase-TiO_2 (JCPDF 21-1272). In addition, the crystallinity of anatase is increased with increasing calcination temperatures from 300 to 550 °C. The content of the amorphous and the anatase phases has been determined in the latter samples by Rietveld analysis of the XRD patterns. The results indicate that the percentage of anatase in the samples calcined at 300, 350, 450, and 550 °C is 0%, 35%, 85%, and 100%, respectively. The rest is amorphous. The average anatase-TiO_2 particle size also increased from 6 to 13 nm, as estimated from the peak width of the anatase (1 0 1) reflection using the Scherrer equation [30]. Interestingly, it is clearly seen that no crystalline Pd phase is formed before the calcination temperature exceeds 450 °C. Thus, at low Pd content (0.5 wt.%) a high dispersion of smaller nanoparticles of Pd within the pores has been obviously achieved.

Fig. 6 shows nitrogen adsorption–desorption isotherms and Barrett–Joyner–Halenda (BJH) pore-size distribution plots of the mesoporous Pd/TiO_2 calcined at different temperatures. All samples show similar type-IV isotherms, typical reversible type IV adsorption isotherms are found for calcined samples from 300 to 450 °C and the main pore diameters are 6–8 nm. The sharpness of the inflection resulting is characteristic for mesopores ordered in two-dimensional hexagonal symmetry. For calcined samples at 500 and 550 °C, the hysteresis loop is broader and shifts to higher relative pressure (Fig. 6). This broadening and shifting indicates the loss

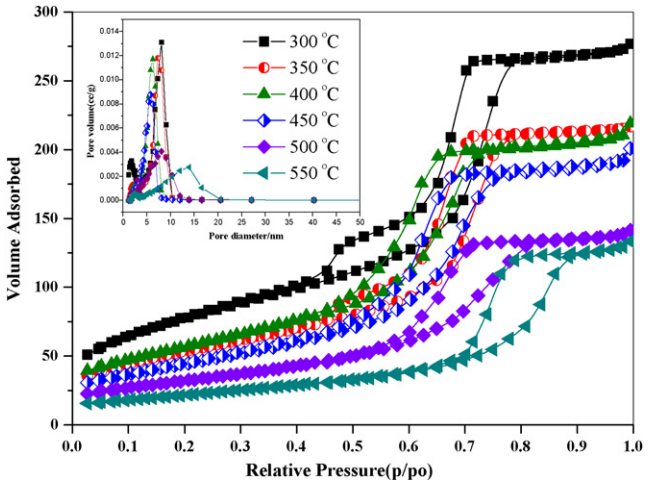

Fig. 6. N_2 sorption isotherms and pore size distributions (inset) of the mesoporous of Pd/TiO_2 calcined at 300 °C, 350 °C, 400 °C, 450 °C, 500 °C and 550 °C. (Adapted with permission from ref. [20]. Copyright 2010 American Chemical Society)

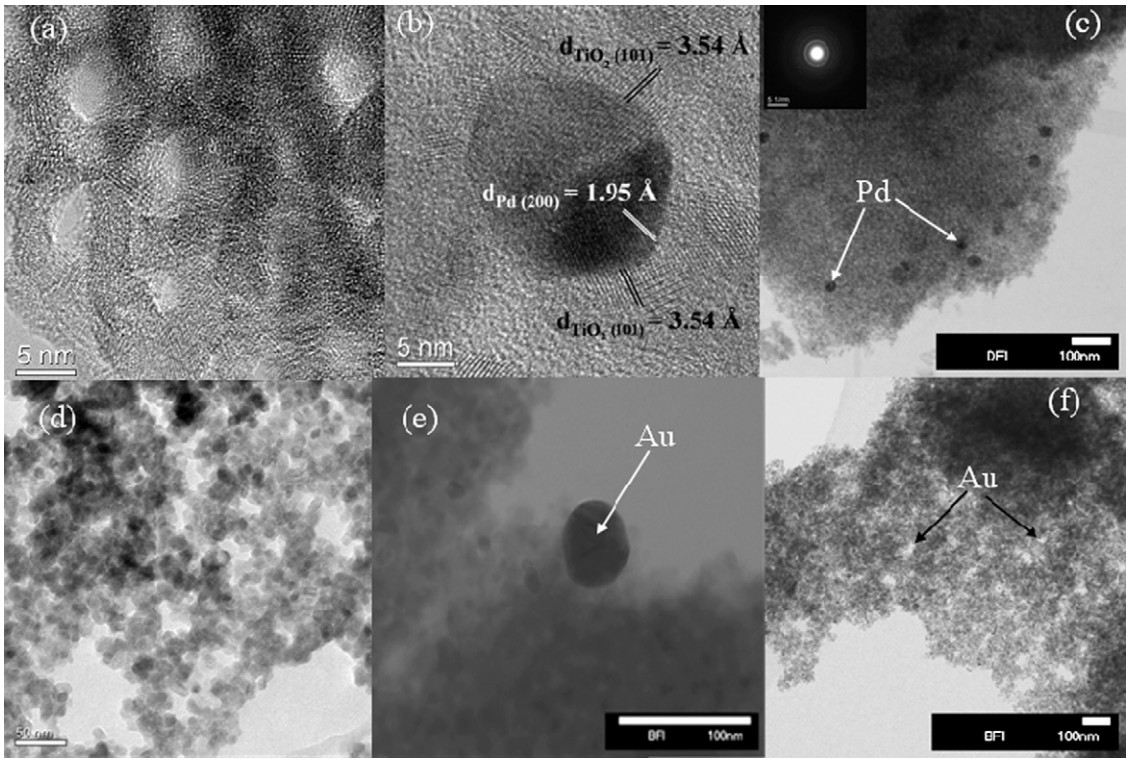

Fig. 7. TEM images of two-dimensional hexagonal mesoporous Pd/TiO_2 nanocomposites calcined at 350 °C (a), HRTEM image of Pd cubooctahedron using the (2 0 0) reflection beams and TiO_2 anatase phase using (1 0 1) calcined at 450 °C (b), the dark-field TEM image of Pd/TiO_2 calcined at 450 °C (c), The insets show the SAED patterns for the anatase phase at 450 °C. TEM image of Au/TiO_2 calcined at 450 °C for 4 h (d), the particles are not agglomerated and quite uniform in size and shape. BF-TEM of 0.5 wt.% Au/TiO_2 nanoparticles (e) and (f). Either Au or Pd particles are highly dispersed onto the TiO_2 mesoporous with an average particle size of ~20–25 nm. (Reprinted in part with permission from ref. [20]. Copyright 2010 American Chemical Society).

in long-range ordering of the mesopores and the hysteresis loop can instead be interpreted as resulting from the voids between non-ordered particles. The main pore sizes increased to 12.6 nm upon calcination of the Pd/TiO_2 nanoarchitectures to 550 °C. In addition, the specific surface area of the calcined sample at 300 °C is 223 $m^2\ g^{-1}$ and is subsequently reduced to 78 $m^2\ g^{-1}$ as a result of calcination at temperatures of 550 °C.

Fig. 7 displays the TEM images of the mesoporous Au and Pd/TiO_2 nanocomposites for samples calcined at 350 and 450 °C. Fig. 7a shows a well-defined 2D hexagonal mesostructure of Pd/TiO_2 samples calcined at 350 °C, evincing the formation of a highly ordered mesostructure, which is consistent with the analysis of the SAXRD (Fig. 4a). As seen in the HRTEM images (Fig. 4b) the atomic planes of the Pd particles are separated by 1.95 Å, which agrees with the (2 0 0) lattice spacing of face-centered cubic Pd [31]. Both sorts of nanoparticles, TiO_2 and Pd, are partly in close contact as seen most impressively in Fig. 7e; the lattice fringes exhibit the typical distances, i.e., Pd (2 0 0) (1.95 Å), Pd (1 1 1) (2.24 Å) and TiO_2 (1 0 1) (3.54 Å). Furthermore, TEM images (Fig. 7c and f) of mesoporous Au and Pd/TiO_2 clearly show that the Au and Pd nanoparticles are highly dispersed in the mesoporous TiO_2 network and exhibit diameters of ~20–25 nm. The Au and Pd nanoparticles are found to be much larger than the TiO_2 nanocrystals (Fig. 7c and e). Selected area electron diffraction (SAED) pattern (Fig. 7c inset) further confirm that anatase nanocrystallites are formed. The formed anatase particles are only slightly agglomerated and quite uniform in size and shape and the particle size of these TiO_2 nanocrystals has been measured to be within ~10 nm (Fig. 7d). It is important to note that the incorporation of Au and Pd nanoparticles into the TiO_2 framework does not completely destroy the latter's mesostructure.

3.2. Photocatalytic activity

Anatase nanoparticles, anatase/brookite mixtures, and brookite nanorods: the photocatalytic activity of the tailored anatase/brookite mixtures has been assessed by determining the photonic efficiencies of the degradation of dichloroacetic acid (DCA) in aqueous solution and of the molecular hydrogen production from aqueous methanol solutions, respectively. The photocatalytic degradation of DCA as model pollutant was performed at pH 3 using a pH-stat technique [26]. The photonic efficiencies (ζ) of the photocatalytic degradation of DCA were calculated as the ratio of the initial degradation rate of DCA and the incident photon flux [28,32,33]. The correlation between the surface area of anatase nanoparticles, of anatase/brookite, and of brookite nanorods and the photonic efficiencies was investigated (cf. Fig. 8). As shown in Fig. 8a, a good correlation between the photonic efficiency of the DCA degradation and the surface area is observed, despite the fact that the content of the brookite phase in the investigated powders is varied. With increasing brookite content in the investigated powders, the photonic efficiency decreases (cf. Fig. 8b). Thus, the decrease of the photocatalytic activity in this case can be attributed to the decrease of the surface area and/or to the increase of brookite ratio in the investigated powders. It is often assumed that the larger the specific area, and thus the higher the adsorption of the organic molecules, the higher will be the photocatalytic degradation rate. However, the observed differences in photocatalytic activity, in general, cannot be interpreted using only a single property of the photocatalysts [34]. The photonic efficiencies of DCA degradation have been compared with those of TiO_2 P25. The results reveal that anatase nanoparticles exhibit higher photonic efficiency than TiO_2 P25

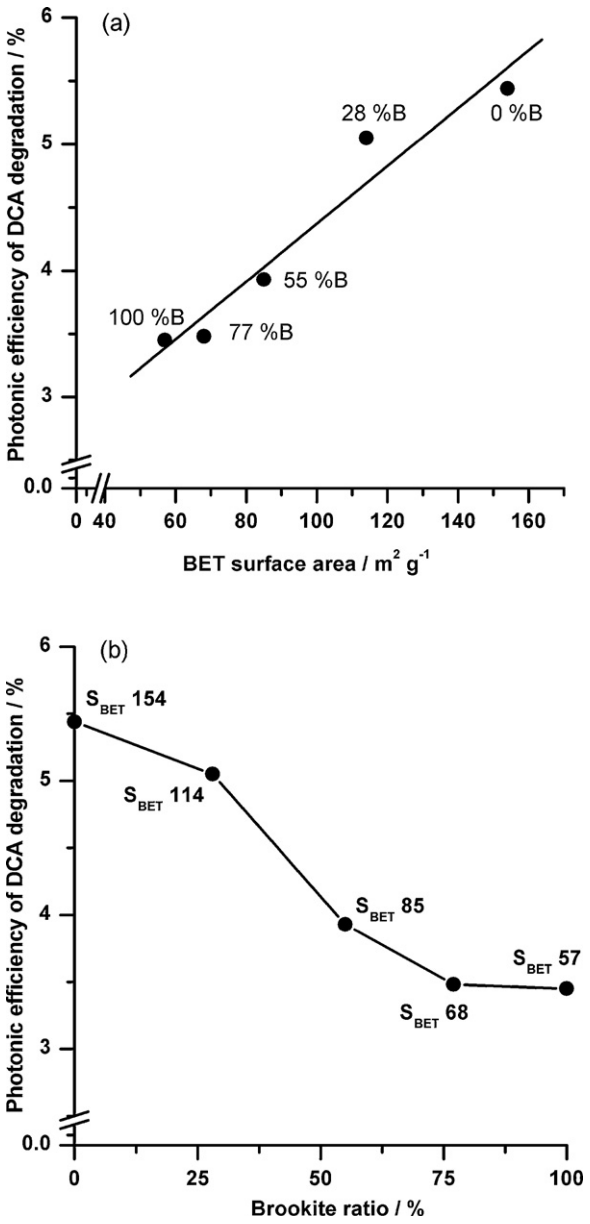

Fig. 8. Correlation between the BET surface area (a), the brookite ratio (b), and the photonic efficiency of DCA degradation. Conditions: 0.5 g l^{-1} catalyst, 60 ml aqueous 1 mmol l^{-1} DCA, and pH 3. Labels B and S_{BET} indicate the content of brookite in percentage (the rest is anatase) and the BET surface area in m^2 g^{-1}. (Adapted with permission from ref. [21]. Copyright 2010 American Chemical Society).

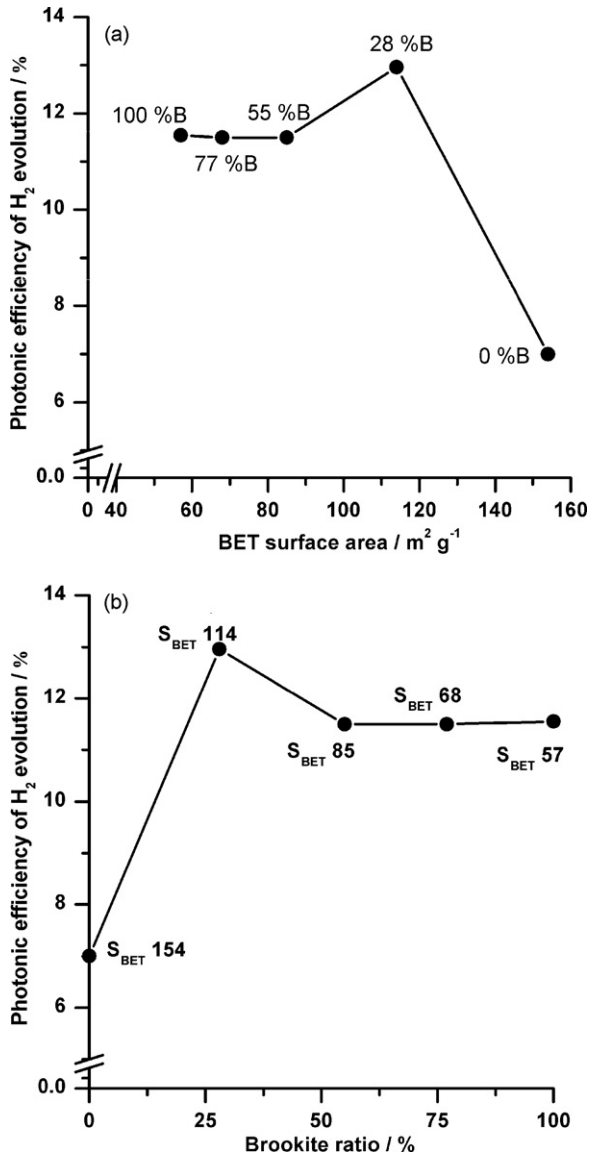

Fig. 9. Correlation between the BET surface area (a), the brookite ratio (b), and the photonic efficiency of H_2 evolution from aqueous methanol solution. Conditions: 0.5 g l^{-1} catalyst, 75 ml aqueous methanol solution (4.93 mol l^{-1}), 0.5 wt.% Pt, UG1 Black filter. Labels B and S_{BET} indicate the content of brookite in percentage (the rest is anatase) and the BET surface area in m^2 g^{-1}, respectively. (Adapted with permission from ref. [21]. Copyright 2010 American Chemical Society).

whereas anatase/brookite mixtures and pure brookite have lower photonic efficiencies than TiO_2 P25.

Prior to the photocatalytic hydrogen evolution tests, the TiO_2 powders have been loaded with 0.5 wt.% Pt nanoparticles using colloidal Pt solution. Colloidal Pt solution have been used to avoid the probability of the change of the particle size of the Pt nanoparticles during the Pt loading to ensure that the difference in the photocatalytic activity can clearly be attributed to the properties of the tested TiO_2 powders. When TiO_2 absorbs a photon the energy of which exceeds its bandgap energy, an electron (e^-)/hole (h^+) pair is generated. Both e^- and h^+ can migrate to the TiO_2 surface and react with adsorbed reactants in a photocatalytic process, or they may undergo an undesired recombination. In the presence of an electron donor, such as methanol, and in the absence of O_2, the excess holes will be consumed and the photogenerated electrons will be trapped near the surface forming tri-valent titanium (Ti^{3+}) instead of reducing H^+. This phenomenon has been observed by Bahnemann et al. [35] in laser-flash photolysis experiments employing suspensions of colloidal TiO_2. Loading the TiO_2 surface with small Pt islands creates sinks for the electrons thus facilitating the separation of e^-/h^+ pairs photogenerated in TiO_2 and promoting the formation of H_2 gas [36–38].

The photonic efficiencies (ζ) of molecular hydrogen production have been calculated by dividing the rate of hydrogen evolution by the photon flux ($\zeta = R/I_0$) [28,32,33]. The rate of hydrogen evolution has been calculated from the slope of the time course of the hydrogen production upon UV-vis illumination. The photon flux has been calculated by employing ferrioxalate actinometry performed under the same conditions as the rate of hydrogen evolution measurements to eliminate any errors associated with the influence of light reflections and reactor geometry. Fig. 9a shows the relation between the surface areas of anatase nanoparticles, of anatase/brookite mixtures, and of brookite nanorods and the

photonic efficiencies of the photocatalytic hydrogen production. As obvious from Fig. 9a no correlation is observed. Surprisingly, there is a reverse dependency between the photonic efficiencies of photocatalytic hydrogen production and the BET surface areas of the investigated powders relative to the brookite content. As the brookite content increases in the investigated powders, the photonic efficiency increases, followed by a slight decrease and subsequently a leveling off despite the simultaneous decrease of the surface area (cf. Fig. 9b). For the TiO_2 powders investigated here, there is no apparent change in the primary particle size for anatase nanoparticles and for brookite nanorods as concluded from the measured crystallite sizes (see Fig. 2). Thus, it becomes obvious that the increased photocatalytic activity of anatase/brookite mixtures and of pure brookite nanorods relative to that of anatase nanoparticles can be explained neither by surface area nor by the primary particle size. However, it seems reasonable that the larger crystallite size of brookite nanorods in comparison with that of the anatase nanoparticles should be regarded as a reason for the increased photocatalytic activity. This large crystallite size might lead to a low density of crystalline defects; hence, it will increase the photocatalytic activity of H_2 evolution from aqueous methanol solution [39]. In fact, the dependence of the photocatalytic activity on the physical properties is indeed very complex [34,40].

The examination of the flatband potential of the different TiO_2 phases should be helpful to understand the above described behavior. In general, the potential of the valance band of TiO_2 (~ + 3.0 V vs. NHE) is considerably more positive than the potential required for methanol oxidation (+1.24 V vs. NHE) [37]. In contrast, the potential of the conduction band electrons in the anatase phase is only positioned by approximately 200 mV more negatively than the potential required for the hydrogen evolution, whereas, in case of rutile, it almost coincides with the potential required for the hydrogen evolution [41,42]. Any further cathodic shift of the flatband potential of TiO_2 will therefore favor reduction reactions initiated by the conduction band electrons such as the photocatalytic hydrogen production. Recently, the conduction band potential of anatase nanoparticles and brookite nanorods have been measured employing impedance measurement under dark condition and photoelectrochemical measurement under illumination condition [21]. It was observed that the conduction band of brookite TiO_2 is positioned by about 140 mV more cathodically than that of the anatase phase. Thus, in the case of the brookite nanorods, the driving force for the proton reduction is higher than that in the case of the anatase nanoparticles. This might also explain why anatase/brookite mixtures and pure brookite nanorods exhibit higher photocatalytic activity than anatase nanoparticles despite of their decreasing surface area.

Since the conduction band of brookite TiO_2 is positioned by about 140 mV more cathodically than that of anatase, this also should facilitate interfacial electron transfer while the resulting energy barrier would suppress back electron transfer. Consequently, the holes left in the valance band of brookite efficiently oxidize organic substrates, while the electrons that have been transferred into the anatase phase are consumed by the reduction of H^+ at the Pt nanoparticles. This will lead to a better charge carrier separation and hence to an increase of the photocatalytic activity similar to that usually assumed for anatase/rutile mixtures [43,44]. The proposed pathway of electrons during photocatalytic H_2 evolution over a mixture of anatase and brookite is illustrated in Fig. 10. The photonic efficiencies of photocatalytic H_2 evolution have been compared with those of TiO_2 P25 under the same conditions. The results reveal that the newly synthesized TiO_2 photocatalysts (anatase/brookite mixtures and pure brookite) exhibit considerable higher activity than TiO_2 P25. For example, the TiO_2 photocatalyst (72% anatase and 28% brookite) has a photonic efficiency twice as high than that of TiO_2 P25.

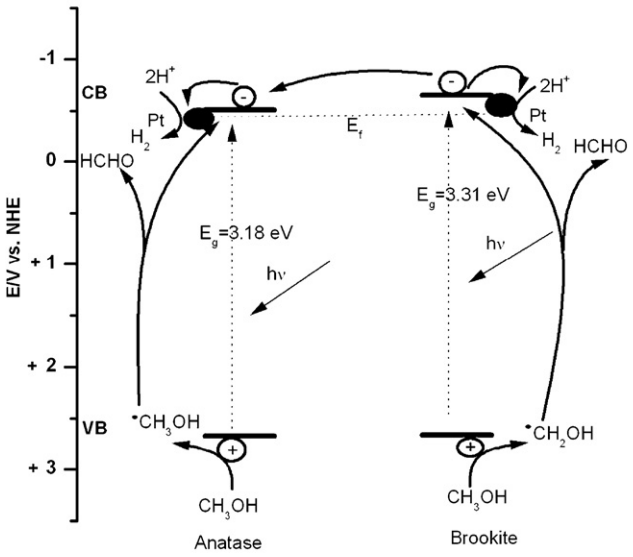

Fig. 10. The proposed pathway of electrons during photocatalytic H_2 evolution over a mixture of anatase and brookite TiO_2 nanomaterials.

Lakshminarasimhan et al. [45,46] have reported that TiO_2 photocatalysts consisting of mesoporous structure showed enhanced photocatalytic activity for H_2 production. These authors ascribed the enhanced photocatalytic activity of such materials to the compact and dense packing of TiO_2 nanoparticles forming a uniform agglomerate, which enables efficient charge separation through interparticle charge transfer. Considering these results and the results reported here, one can predict that the preparation of TiO_2 brookite nanomaterials with such design should result in considerably high photocatalytic H_2 production activity.

Mesoporous TiO_2 photocatalysts: the photocatalytic efficiencies of the newly synthesized 3D Pd/TiO_2 nanocomposites calcined at temperatures between 300 and 550 °C for the photooxidation of aqueous solutions of CH_3OH [30 mmol l^{-1}] to HCHO have been studied (Fig. 11). The results indicated that with increasing the calcinations temperatures from 350 to 550 °C, the photonic efficiencies are increasing from 10.5% to 16.3% (Fig. 11). It is clearly

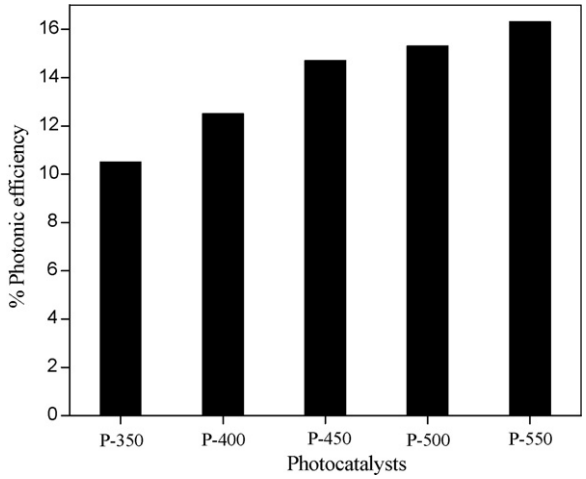

Fig. 11. Photonic efficiency of HCHO formation over mesostructured Pd/TiO_2 nanocomposites calcined at 350 °C, 400 °C, 450 °C, 500 °C and 550 °C. Photocatalyst loading, 1 g l^{-1}; 30 mol l^{-1} aqueous solution of CH_3OH (O_2 saturated, natural pH; T = 20 °C); reaction volume, 75 ml; $I_0 = 4.49 \times 10^{-6}$ einstein l^{-1} s^{-1} (ca. >320 nm).

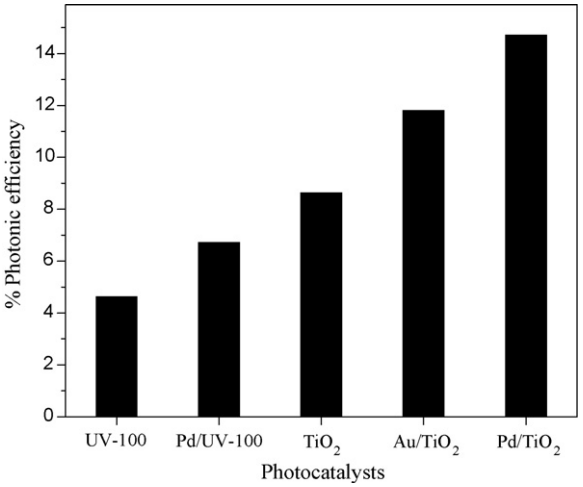

Fig. 12. Photonic efficiency of HCHO formation over commercial photocatalyst UV-100, photodeposited Pd/UV-100, mesostructured pure TiO_2, Au/TiO_2 and Pd/TiO_2 nanocomposites calcined at 450 °C. Photocatalyst loading, 1 g l^{-1}; 30 mmol l^{-1} aqueous solution of CH_3OH (O_2 saturated, natural pH; T = 20 °C); reaction volume, 75 ml; $I_0 = 4.49 \times 10^{-6}$ einstein l^{-1} s^{-1} (ca. >320 nm).

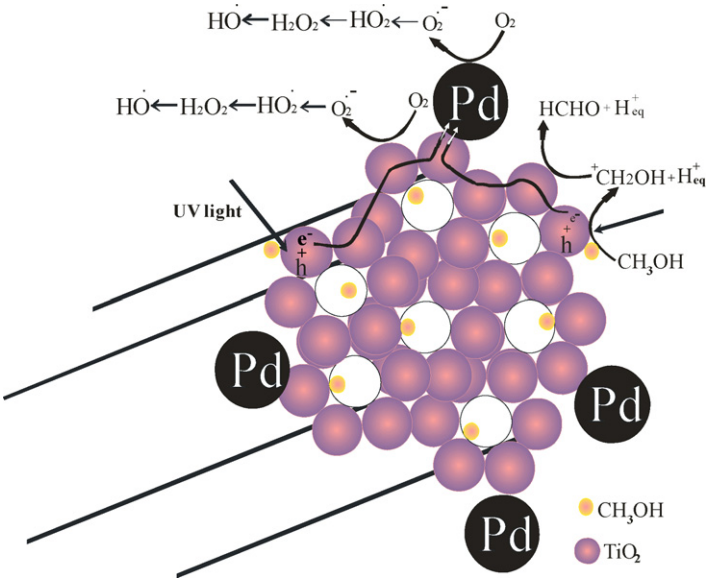

Scheme 1. Proposed antenna and reaction mechanisms for methanol photooxidation to illustrate the enhanced photonic efficiency of mesostructured Pd/TiO_2 photocatalysts, absorption of UV light by the semiconducting nanoparticle promotes an electron from the valence band to the conduction band. The lines in the scheme show a cut perpendicular to the *c* axis of the hexagonal pore system which extends infinitely in this direction. (Reprinted with permission from ref. [20]. Copyright 2010 American Chemical Society).

seen from WAXRD that the crystallinity increases by a factor of 4 when the samples are calcined at 550 °C rather than at 350 °C whereas the increase in photonic efficiencies is smaller than 50%. Considering the larger internal surface area (163 m^2 g^{-1}) of P-450 as compared with the surface area of P-550 (78 m^2 g^{-1}), in P-450 most of the anatase phase exists as nanoparticulate bricks forming the pore walls. Hence, the photocatalytic •OH production must occur mainly on an internal surface. Furthermore, CH_3OH adsorption onto P-450 should take place mainly within the pores of this high surface area material. Therefore, it can be expected that the concentration of CH_3OH inside the pores will be higher in the latter samples as compared with those achievable for P-550. The slightly higher HCHO formation rate found on P-550 can be explained by its much higher crystallinity as compared with P-450 (Figs. 5 and 11). These crystalline anatase particles are believed to be responsible for the production of reactive •OH radicals, the formation probability of which should thus be much higher for P-550. Moreover, the high photocatalytic activity of P-350 is surprising since its crystallinity is by a factor of more than two weaker than that of P-450. The higher BET surface area of P-350, which exceeds that of P-450 by 30%, cannot explain the good photocatalytic performance alone because Pd/UV-100 has a similar surface area (225 m^2 g^{-1}). The latter is, however, by a factor of 1.5 photocatalytically less active. Therefore, we suggest that the well-ordered mesostructure of P-350 supports the transport properties of all reactants involved in the photocatalytic process and, thus, enhances the overall activity. The good photocatalytic performance of P-550, on the other hand, indicates that a highly ordered mesoporous system is not a prerequisite for high photocatalytic activity. However, both P-350 and P-450 must be considered as economically more viable photocatalysts as compared to P-550 since for their preparation energy can be saved in the calcination step.

For comparison between commercial photocatalysts pure UV-100 and Pd photodeposited/UV-100 and mesostructured pure TiO_2, Au/TiO_2 and Pd/TiO_2 nanocomposites calcined at 450 °C, the photonic efficiencies have been calculated by determination the rate of HCHO formation generated by the photocatalytic oxidation of CH_3OH (Fig. 12). The results revealed that the addition of precious metals is improving the photonic efficiency in both cases, i.e., for UV-100 as well as for mesoporous TiO_2. Also, the photocatalytic activities of the hexagonally mesostructured pure TiO_2, Au/TiO_2 and Pd/TiO_2 exceed that of Pd/Hombikat UV-100 [20], although the Hombikat TiO_2 material was calcined at 450 °C and is, thus, much more crystalline than most of newly prepared mesostructured Pd/TiO_2. This difference cannot be explained by different surface areas, because this is even higher for the Hombikat material (225 m g^{-1}). Such high photonic efficiencies of the mesoporous Pd/TiO_2 as compared with Pd/Hombikat UV-100 can be attributed to several effects, such as a lower light scattering effect of the ordered mesopores, an accumulated local concentration of •OH [47], or a fast transport of the target molecule CH_3OH to the active sites due to the facile diffusion of the CH_3OH through the ordered porous network, which for the Hombikat UV-100 reference sample is hindered by the heterogeneities existing in the bulk sample.

According to the above data analysis the following mechanism is suggested (see Scheme 1). The 3D mesoporous TiO_2 network acts as an antenna system transferring the initially generated electrons from the location of light absorption to a suitable interface with the noble metal catalyst where the actual electron transfer reaction will take place [19,20,37,48]. Within this antenna model, it can be envisaged that the overlap of the energy bands of the nanoparticles forming this network will result in unified energy bands for the entire system enabling a quasi-free movement of the photogenerated charge carriers throughout. Consequently, an electron generated by light absorption within one of the nanoparticles forming the network will subsequently be available to promote redox processes anywhere within the structure. Assuming a Schottky contact between the mesoporous TiO_2 network and the noble metal particle, the Au or Pd particles then serve as active sites for the reduction of molecular O_2, on which the trapped photogenerated electrons are transferred to O_2 producing $O_2^{\bullet-}$ radicals. It should be noted that it is frequently overseen that this latter process is really the "bottle-neck" in most photocatalytic transformations being the rate-determining step due to its very small thermodynamic driving force. Thus, its acceleration through the electron transfer catalysis induced by the Au or Pd deposits will result in the observed increase in the yield of the photocatalytic methanol oxidation.

4. Conclusions

Anatase nanoparticles, tailored anatase/brookite mixtures, and pure brookite TiO_2 nanorods have been synthesized via a simple hydrothermal method employing aqueous solutions of the titanium(IV) bis(ammoniumlactate) dihydroxide complex in the presence of urea as OH^- source. The photocatalytic activities of these materials have been assessed by the photocatalytic degradation of dichloroacetic acid (DCA) in aqueous suspension and by the photocatalytic H_2 evolution from aqueous methanol solutions. The results revealed that anatase nanoparticles exhibit higher activity than anatase/brookite mixtures and pure brookite nanorods and even higher than TiO_2 P25 for the photocatalytic degradation of DCA. In contrary, anatase/brookite mixtures and pure brookite nanorods exhibit considerable higher activity than anatase nanoparticles and even than TiO_2 P25 for the photocatalytic H_2 evolution, despite the fact that the former exhibits lower surface areas. This behavior can be explained by the fact that the flatband potential of the brookite nanorods is shifted by 140 mV more cathodically than the flatband potential of the anatase nanoparticles and/or by the better charge carrier separation in the case of anatase/brookite mixtures. Beside the effect of the phase composition on the photocatalytic activity of titania-based photocatalysts, the effect of the mesoporous order has also been investigated. Highly ordered hexagonal *P6m* mesoporous structures of Au or Pd/TiO_2 nanocrystals have been synthesized through simple one-step sol–gel reactions in the presence of a F127 triblock copolymer as the template to direct the formation of nanostructured photocatalysts. The formed anatase particles are only slightly agglomerated and quite uniform in size and shape. Hexagonal *P6m* mesoporous Au and Pd/TiO_2 nanoarchitectures showed ~3–4 times higher activity for the photooxidation of CH_3OH than Pd photodeposited on commercial Hombikat UV-100. The increased HCHO formation rate revealed that the photocatalytic oxidation efficiencies within the mesoporous Pd/TiO_2 system is (in spite of its lower surface area) superior to that of Pd/UV-100. The key to this success is the preparation of Pd/TiO_2 networks with an ordered mesoporous structure which at the same time render the methanol diffusion into the bulk of the photocatalysts facile and hence provide fast transport channels for the methanol molecules.

Acknowledgements

A.A.I. acknowledges the Alexander von Humboldt (AvH) Foundation for granting him a research fellowship. T.A.K. thanks the Egyptian Ministry of Higher Education for granting him a doctoral scholarship.

References

[1] H.J. Zhang, G.H. Chen, D.W. Bahnemann, Photoelectrocatalytic materials for environmental applications, J. Mater. Chem. 19 (2009) 5089–5121.
[2] B. Liu, E.S. Aydil, Growth of oriented single-crystalline rutile TiO_2 nanorods on transparent conducting substrates for dye-sensitized solar cells, J. Am. Chem. Soc. 131 (2009) 3985–3990.
[3] T.A. Kandiel, R. Dillert, A. Feldhoff, D.W. Bahemann, Direct synthesis of photocatalytically active rutile TiO_2 nanorods partly decorated with anatase nanoparticles, J. Phys. Chem. C 114 (2010) 4909–4915.
[4] N. Murakami, T. Kamai, T. Tsubota, T. Ohno, Novel hydrothermal preparation of pure brookite-type titanium(IV) oxide nanocrystal under strong acidic conditions, Catal. Commun. 10 (2009) 963–966.
[5] A. Di Paola, M. Addamo, M. Bellardita, E. Cazzanelli, L. Palmisano, Preparation of photocatalytic brookite thin films, Thin Solid Films 515 (2007) 3527–3529.
[6] M. Addamo, M. Bellardita, A. Di Paola, L. Palmisano, Preparation and photoactivity of nanostructured anatase, rutile and brookite TiO_2 thin films, Chem. Commun. (2006) 4943–4945.
[7] J.G. Li, T. Ishigaki, X.D. Sun, Anatase, brookite, and rutile nanocrystals via redox reactions under mild hydrothermal conditions: phase-selective synthesis and physicochemical properties, J. Phys. Chem. C 111 (2007) 4969–4976.
[8] H. Kominami, Y. Ishii, M. Kohno, S. Konishi, Y. Kera, B. Ohtani, Nanocrystalline brookite-type titanium(IV) oxide photocatalysts prepared by a solvothermal method: correlation between their physical properties and photocatalytic activities, Catal. Lett. 91 (2003) 41–47.
[9] B. Ohtani, J. Handa, S. Nishimoto, T. Kagiya, Highly-active semiconductor photocatalyst – extra-fine crystallite of brookite TiO_2 for redox reaction in aqueous propan-2-ol and or silver sulfate-solution, Chem. Phys. Lett. 120 (1985) 292–294.
[10] D.L. Li, H.S. Zhou, I. Honma, Design and synthesis of self-ordered mesoporous nanocomposite through controlled in-situ crystallization, Nat. Mater. 3 (2004) 65–72.
[11] J. Lee, M.C. Orilall, S.C. Warren, M. Kamperman, F.J. Disalvo, U. Wiesner, Direct access to thermally stable and highly crystalline mesoporous transition-metal oxides with uniform pores, Nat. Mater. 7 (2008) 222–228.
[12] M. Niederberger, M.H. Bartl, G.D. Stucky, Benzyl alcohol and titanium tetrachloride – a versatile reaction system for the nonaqueous and low-temperature preparation of crystalline and luminescent titania nanoparticles, Chem. Mater. 14 (2002) 4364–4370.
[13] H. Shibata, T. Ogura, T. Mukai, T. Ohkubo, H. Sakai, M. Abe, Direct synthesis of mesoporous titania particles having a crystalline wall, J. Am. Chem. Soc. 127 (2005) 16396–16397.
[14] S. Ito, T. Takeuchi, T. Katayama, M. Sugiyama, M. Matsuda, T. Kitamura, Y. Wada, S. Yanagida, Conductive and transparent multilayer films for low-temperature-sintered mesoporous TiO_2 electrodes of dye-sensitized solar cells, Chem. Mater. 15 (2003) 2824–2828.
[15] S. Chappel, S.G. Chen, A. Zaban, TiO_2-coated nanoporous SnO_2 electrodes for dye-sensitized solar cells, Langmuir 18 (2002) 3336–3342.
[16] H.X. Li, Z.F. Bian, J. Zhu, Y.N. Huo, H. Li, Y.F. Lu, Mesoporous Au/TiO_2 nanocomposites with enhanced photocatalytic activity, J. Am. Chem. Soc. 129 (2007) 4538–4539.
[17] M. Andersson, H. Birkedal, N.R. Franklin, T. Ostomel, S. Boettcher, A.E.C. Palmqvist, G.D. Stucky, Ag/AgCl-loaded ordered mesoporous anatase for photocatalysis, Chem. Mater. 17 (2005) 1409–1415.
[18] X.C. Wang, J.C. Yu, H.Y. Yip, L. Wu, P.K. Wong, S.Y. Lai, A mesoporous Pt/TiO_2 nanoarchitecture with catalytic and photocatalytic functions, Chem. Eur. J. 11 (2005) 2997–3004.
[19] A.A. Ismail, D.W. Bahnemann, I. Bannat, M. Wark, Gold nanoparticles on mesoporous interparticle networks of titanium dioxide nanocrystals for enhanced photonic efficiencies, J. Phys. Chem. C 113 (2009) 7429–7435.
[20] A.A. Ismail, D.W. Bahnemann, L. Robben, V. Yarovyi, M. Wark, Palladium doped porous titania photocatalysts: impact of mesoporous order and crystallinity, Chem. Mater. 22 (2010) 108–116.
[21] T.A. Kandiel, A. Feldhoff, L. Robben, R. Dillert, D.W. Bahnemann, Tailored titanium dioxide nanomaterials: anatase nanoparticles and brookite nanorods as highly active photocatalysts, Chem. Mater. 22 (2010) 2050–2060.
[22] S.J. Gregg, K.S.W. Sing, Adsorption, Surface Area and Porosity, Academic Press, London, 1982.
[23] T.A. Kandiel, R. Dillert, D.W. Bahnemann, Enhanced photocatalytic production of molecular hydrogen on TiO_2 modified with pt-polypyrrole nanocomposites, Photochem. Photobiol. Sci. 8 (2009) 683–690.
[24] C.G. Hatchard, C.A. Parker, A new sensitive chemical actinometer. 2. Potassium ferrioxalate as a standard chemical actinometer, Proc. R. Soc. Ser. A 235 (1956) 518–536.
[25] A.D. Kirk, C. Namasivayam, Errors in ferrioxalate actinometry, Anal. Chem. 55 (1983) 2428–2429.
[26] D. Bahnemann, D. Bockelmann, R. Goslich, Mechanistic studies of water detoxification in illuminated TiO_2 suspensions, Sol. Energy Mater. 24 (1991) 564–583.
[27] T. Nash, The colorimetric estimation of formaldehyde by means of the hantzsch reaction, Biochem. J. 55 (1953) 416–421.
[28] N. Serpone, R. Terzian, D. Lawless, P. Kennepohl, G. Sauve, On the usage of turnover numbers and quantum yields in heterogeneous photocatalysis, J. Photochem. Photobiol. A: Chem. 73 (1993) 11–16.
[29] J. Fan, S.W. Boettcher, G.D. Stucky, Nanoparticle assembly of ordered multicomponent mesostructured metal oxides via a versatile sol–gel process, Chem. Mater. 18 (2006) 6391–6396.
[30] M.J.B.L.V.Azároff, The Powder Method in X-Ray Crystallography, New York, 1958.
[31] Y.J. Xiong, J.Y. Chen, B. Wiley, Y.A. Xia, Y.D. Yin, Z.Y. Li, Size-dependence of surface plasmon resonance and oxidation for Pd nanocubes synthesized via a seed etching process, Nano Lett. 5 (2005) 1237–1242.
[32] N. Serpone, A. Salinaro, Terminology, relative photonic efficiencies and quantum yields in heterogeneous photocatalysis. Part I: suggested protocol (technical report), Pure Appl. Chem. 71 (1999) 303–320.
[33] A. Salinaro, A.V. Emeline, J.C. Zhao, H. Hidaka, V.K. Ryabchuk, N. Serpone, Terminology, relative photonic efficiencies and quantum yields in heterogeneous photocatalysis. Part II: experimental determination of quantum yields (technical report), Pure Appl. Chem. 71 (1999) 321–335.
[34] B. Ohtani, Preparing articles on photocatalysis – beyond the illusions, misconceptions, and speculation, Chem. Lett. 37 (2008) 217–229.
[35] D. Bahnemann, A. Henglein, J. Lilie, L. Spanhel, Flash-photolysis observation of the absorption-spectra of trapped positive holes and electrons in colloidal TiO_2, J. Phys. Chem. 88 (1984) 709–711.
[36] D. Bahnemann, A. Henglein, L. Spanhel, Detection of the intermediates of colloidal TiO_2-catalyzed photoreactions, Faraday Discuss. 78 (1984) 151–163.
[37] C.Y. Wang, R. Pagel, D.W. Bahnemann, J.K. Dohrmann, Quantum yield of formaldehyde formation in the presence of colloidal TiO_2-based photocata-

lysts: effect of intermittent illumination, platinization, and deoxygenation, J. Phys. Chem. B 108 (2004) 14082–14092.
[38] J. Kiwi, M. Grätzel, Optimization of conditions for photochemical water cleavage – aqueous Pt/TiO_2 (anatase) dispersions under ultraviolet-light, J. Phys. Chem. 88 (1984) 1302–1307.
[39] F. Amano, O.O. Prieto-Mahaney, Y. Terada, T. Yasumoto, T. Shibayama, B. Ohtani, Decahedral single-crystalline particles of anatase titanium(IV) oxide with high photocatalytic activity, Chem. Mater. 21 (2009) 2601–2603.
[40] O.O. Prieto-Mahaney, N. Murakami, R. Abe, B. Ohtani, Correlation between photocatalytic activities and structural and physical properties of titanium(IV) oxide powders, Chem. Lett. 38 (2009) 238–239.
[41] M.V. Rao, K. Rajeshwar, V.R. Paiverneker, J. Dubow, Photosynthetic production of H_2 and H_2O_2 on semiconducting oxide grains in aqueous-solutions, J. Phys. Chem. 84 (1980) 1987–1991.
[42] K.E. Karakitsou, X.E. Verykios, Effects of altervalent cation doping of TiO_2 on its performance as a photocatalyst for water cleavage, J. Phys. Chem. 97 (1993) 1184–1189.
[43] A. Zachariah, K.V. Baiju, S. Shukla, K.S. Deepa, J. James, K.G.K. Warrier, Synergistic effect in photocatalysis as observed for mixed-phase nanocrystalline titania processed via sol–gel solvent mixing and calcination, J. Phys. Chem. C 112 (2008) 11345–11356.
[44] Y.K. Kho, A. Iwase, W.Y. Teoh, L. Madler, A. Kudo, R. Amal, Photocatalytic H_2 evolution over TiO_2 nanoparticles. The synergistic effect of anatase and rutile, J. Phys. Chem. C 114 (2010) 2821–2829.
[45] N. Lakshminarasimhan, E. Bae, W. Choi, Enhanced photocatalytic production of H_2 on mesoporous TiO_2 prepared by template-free method: role of interparticle charge transfer, J. Phys. Chem. C 111 (2007) 15244–15250.
[46] N. Lakshminarasimhan, W. Kim, W. Choi, Effect of the agglomerated state on the photocatalytic hydrogen production with in situ agglomeration of colloidal TiO_2 nanoparticles, J. Phys. Chem. C 112 (2008) 20451–20457.
[47] S. Tojo, T. Tachikawa, M. Fujitsuka, T. Majima, Oxidation processes of aromatic sulfides by hydroxyl radicals in colloidal solution of TiO_2 during pulse radiolysis, Chem. Phys. Lett. 384 (2004) 312–316.
[48] C.Y. Wang, R. Pagel, J.K. Dohrmann, D.W. Bahnemann, Antenna mechanism and deaggregation concept: novel mechanistic principles for photocatalysis, C. R. Chim. 9 (2006) 761–773.